JACS
JOURNAL OF THE AMERICAN CHEMICAL SOCIETY
pubs.acs.org/JACS
Article

Cancer Cell-Selective Membrane Receptor Clustering Driven by VEGF Secretion for *In Vivo* Therapy

Shiyi Bi, Wei Chen, Yanyun Fang, Yingfei Wang, Qing Zhang, Hongqian Guo, Huangxian Ju, and Ying Liu*

Cite This: *J. Am. Chem. Soc.* 2023, 145, 5041−5052
Read Online
ACCESS | Metrics & More | Article Recommendations | Supporting Information

ABSTRACT: Clustering of cell membrane receptors regulates cell behaviors. Although receptor clustering plans have achieved wide applications in cancer therapy, it still remains challenging to manipulate receptor clustering selectively for cancer cells with little influence on normal cells. Here, we design a Raji cell Selective MAnipulation of Receptor Clustering (SMARC) strategy for CD20, which is driven by endogenous secretion of Raji cells. Retractable DNA nanostrings with repeating hairpin-structured units are anchored to the cell membrane CD20, which contract in response to Raji cell-secreted vascular endothelial growth factor (VEGF) with corresponding CD20 clustering. The contraction of DNA nanostrings is intensified via a VEGF amplifier including DNA cyclic reactions to continuously trigger the foldings of hairpin-structured units in DNA nanostrings. The SMARC strategy shows selective and efficient apoptosis of Raji cells with little interference to normal B cells and demonstrates good *in vivo* therapeutic efficacy, which provides a promising tool for precise cancer therapy.

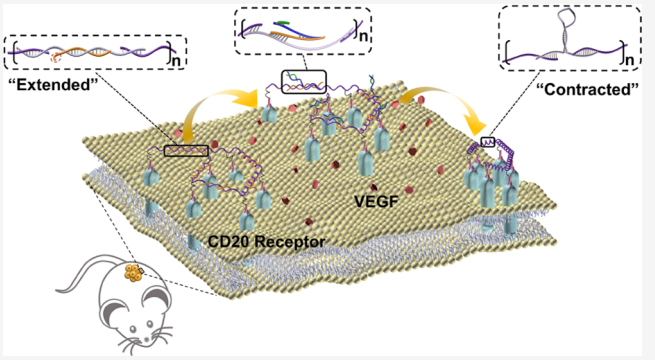

INTRODUCTION

Cell membrane receptors sense extracellular stimuli and accordingly result in cellular signaling cascades.[1−3] Manipulating receptor oligomerization can activate downstream signaling pathways,[4] therefore playing important roles in regulating cell behaviors, including immune activation,[5] intercellular communication,[6] proliferation, and apoptosis.[7] Functionalized proteins,[8] polymers,[9] as well as *in situ* polymerization[10,11] and peptide self-assembly[12] have been successfully applied to generate membrane receptor clustering. However, the clustering processes mainly rely on receptors' undirected migration and random collision at the cell membrane. The lack of active manipulation impairs clustering efficiency.[13]

With the precise sequence design and programmable configurational change, the DNA nanoscaffold is a preferred tool to control membrane receptor clustering.[14−18] External light stimulation[19] or addition of trigger DNA strands[2] could fold hairpin structures in DNA nanoscaffolds, correspondingly causing their spring-like movements, which actively and efficiently manipulated receptor clustering. However, cell-selective manipulation is still difficult to achieve. Taking lymphoma for example, its current therapeutic plans mainly rely on the anti CD20 monoclonal antibody to recognize the membrane receptor CD20.[20,21] However, since CD20 is also expressed by normal B lymphocytes and is involved in many signaling pathways of normal physiological processes,[22] indiscriminately generating CD20 clustering would impair therapeutic efficiency and bring side effects. Therefore, it is crucial to develop receptor clustering strategies selectively for cancer cells in precise cancer therapy.

Vascular endothelial growth factor (VEGF) is a signaling protein that cells secrete to promote new blood vessel growth.[23] Due to its relatively higher expression around cancer cells than normal cells, which is sufficient for cell discrimination,[24] it has been extensively studied as a cancer biomarker[25,26] and therapeutic target[27,28] for tumor therapeutic plans.[29,30] This makes VEGF an appropriate candidate to trigger cancer cell-selective membrane receptor clustering. However, as an endogenously produced substance, *in vivo* VEGF concentration is still too low to generate effective receptor clustering compared with externally exerted stimuli. Here, we develop a Selective MAnipulation of Receptor Clustering (SMARC) strategy to regulate CD20 clustering selectively for Raji cells, which achieves efficient Raji cell apoptosis and *in vivo* therapy. A retractable DNA nanostring is

Received: September 30, 2022
Published: February 23, 2023

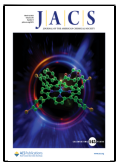

https://doi.org/10.1021/jacs.2c10428
J. Am. Chem. Soc. 2023, 145, 5041−5052

Scheme 1. Schematic Illustration of the SMARC Strategy for Membrane Receptor Clustering Selectively on Raji Cells[a]

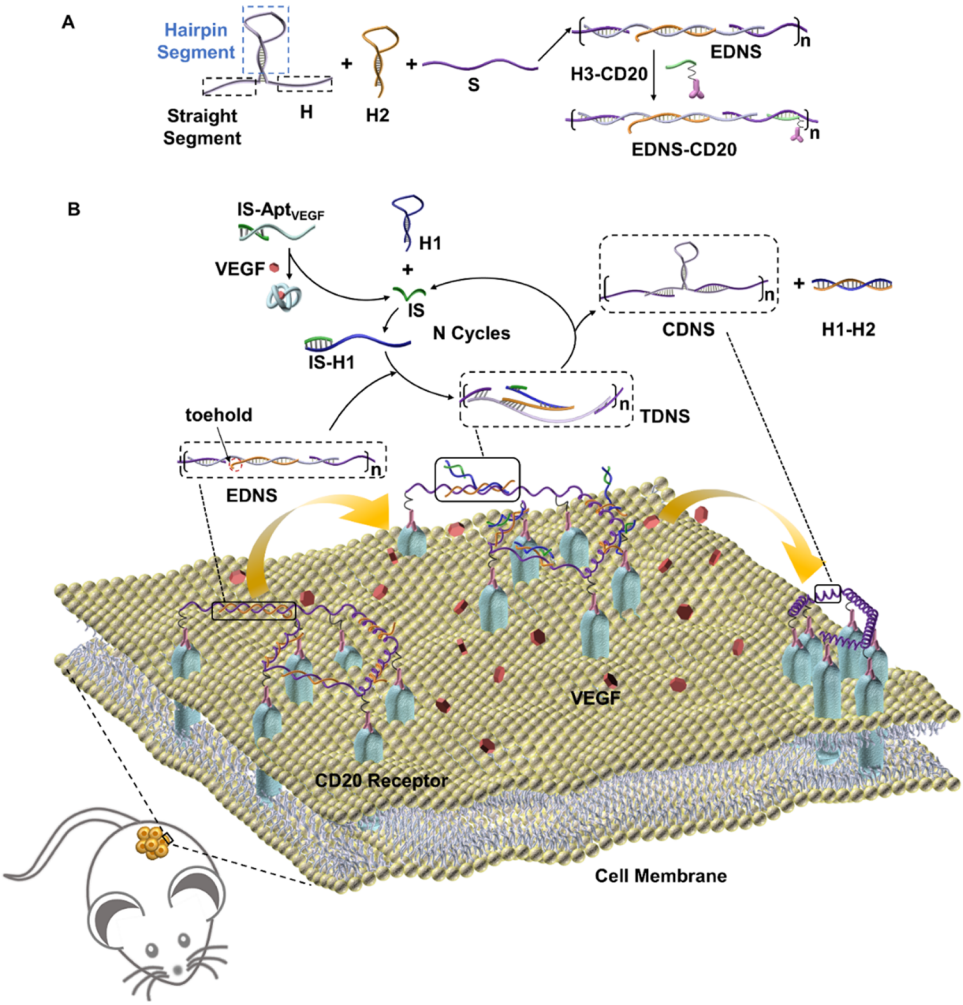

[a](A) Synthesis of EDNS-CD20. (B) VEGF amplified DNA nanostring contraction and corresponding CD20 clustering on the Raji cell membrane for cancer therapy.

designed and coupled with a VEGF amplifier to perform the SMARC strategy. Through the hybridization chain assembly of DNA strands S, H, and H2, the DNA nanostring is synthesized with an extended configuration (extended DNA nanostring, EDNS). The DNA strand H contains two segments, the "straight" segment hybridizing with S to build the nanostring skeleton and the "hairpin" segment hybridizing with H2 to stretch the nanostring into an "extended" configuration. To anchor EDNS on the Raji cell membrane, it is also hybridized with the CD20 antibody conjugated DNA strand (H3-CD20) to obtain the CD20 antibody conjugated DNA nanostring (EDNS-CD20) (Scheme 1A). The hairpin segment with 27 bp and numerous repeating unit S/H provide the DNA nanostring (DNS) with sufficient length difference between EDNS and CDNS (contracted DNA nanostring) configurations.

Subcutaneous Raji lymphoma was chosen as the tumor model for the SMARC strategy to demonstrate selective CD20 clustering in response to VEGF secretion. After intravenous injection, EDNS-CD20 recognizes the CD20 receptor and binds to the Raji cell membrane. The VEGF amplifier is composed of a duplex DNA strand IS-Apt$_{VEGF}$ and a cyclic reaction among DNA strands H1, IS, and the DNA nanostring. IS-Apt$_{VEGF}$ recognizes and binds with VEGF that is secreted from Raji cells and releases the DNA strand IS. IS subsequently hybridizes with the DNA strand H1 to unfold its hairpin structure. The as-obtained IS-H1 duplex acts as a trigger for the configuration change of the DNA nanostring: IS-H1 hybridizes with EDNS via the toehold in H2 and generates the DNA nanostring in the transient state (TDNS). The strand displacement reaction between IS-H1 and H2 continuously proceeds, which pulls H2 away from the DNA nanostring, therefore recovering the hairpin structure of H and converting the DNA nanostring to a contracted configuration (CDNS). The H1−H2 duplex is also produced as a reaction product with the release of free IS to complete the cyclic reaction. The regenerated IS continuously hybridizes with H1 for numerous reaction cycles, which amplifies VEGF response and results in efficient DNA nanostring contraction with CD20 receptors clustering at the cell membrane (Scheme 1B). Binding with IS-Apt$_{VEGF}$ also inactivates VEGF, which prevents VEGF receptor (VEGFR) activation and also contributes to tumor therapy. The as-presented SMARC strategy barely demonstrates nonspecific damage to normal B cells that also express CD20 on the membrane with 91% cell viability while achieving effective Raji cell apoptosis and *in vivo* antitumor effects, providing a solution for highly selective treatment.

https://doi.org/10.1021/jacs.2c10428
J. Am. Chem. Soc. 2023, 145, 5041−5052

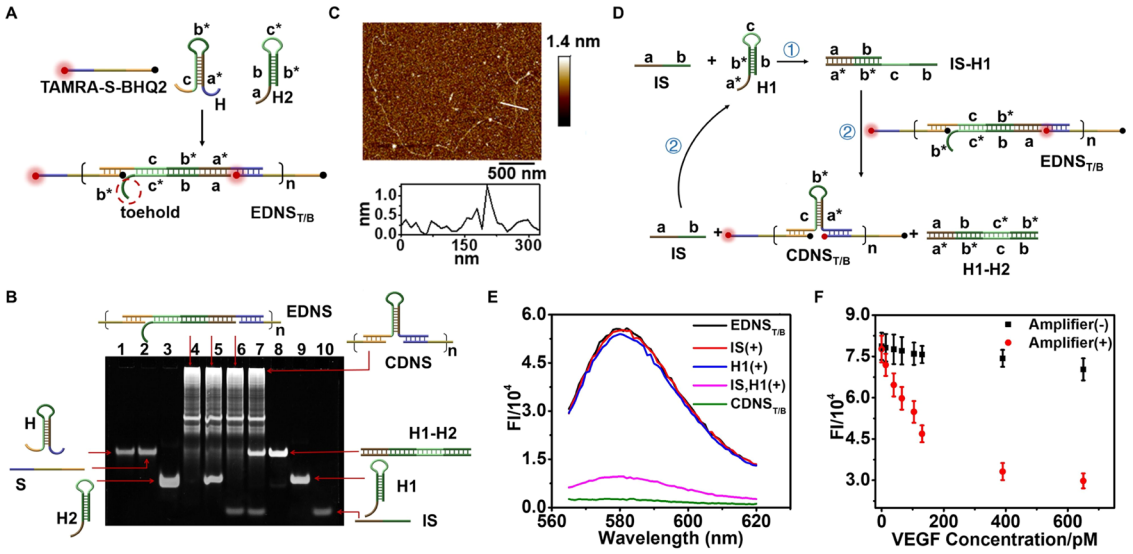

Figure 1. EDNS synthesis and VEGF-responsive configuration change. Schematic illustrations of (A) EDNS$_{T/B}$ synthesis and (D) cyclic reaction for IS, H1, and DNA nanostrings with structure conversion of EDNS$_{T/B}$ to CDNS$_{T/B}$. (B) PAGE characterization of EDNS synthesis and configuration change between EDNS and CDNS. Lane 1: H; Lane 2: S; Lane 3: H2; Lane 4: annealing of H, S, and H2; Lane 5: EDNS in response to H1; Lane 6: EDNS in response to IS; Lane 7: EDNS in response to IS and H1; Lane 8: H1−H2; Lane 9: H1; Lane 10: IS. (C) AFM image of EDNS and the cross-section profile of the white line. (E) Fluorescence spectra of CDNS$_{T/B}$, EDNS$_{T/B}$, and EDNS$_{T/B}$ in response to IS (IS (+)), H1(H1 (+)) and both H1 and IS (H1, IS (+)). The excitation wavelength is 550 nm. (F) Fluorescence intensities of EDNS$_{T/B}$ in response to various concentrations of VEGF in the presence of IS-Apt$_{VEGF}$/H1 (Amplifier (+)) or IS′-Apt$_{VEGF}$/H1′ (Amplifier (−)).

RESULTS AND DISCUSSION

EDNS was synthesized by alternate hybridizing of the DNA strands S, H2, and the hairpin-structured DNA strand H. Segments abc* in H2 have a complementary sequence with the loop and stem in H (a*b*c), which kept EDNS in an extended configuration and left segment b* unpaired in EDNS as a toehold for subsequent displacement reaction (Figure 1A, EDNS$_{T/B}$). The successful synthesis of EDNS was characterized by polyacrylamide gel electrophoresis (PAGE), which showed new bands with much lower mobilities upon annealing DNA strands H, S, and H2 (Figure 1B, lane 4). Multiple bands with lower molecular weight were generated due to different hybridization efficiencies. Atomic force microscopy (AFM) images showed a linear DNA long strand with ∼1.5 nm in height, which corresponded to the height of the double-strand DNA (Figure 1C), further confirming the successful generation of EDNS. The as-obtained EDNS is 4580 nm for AFM characterization, and its components H, H2, and S contain 62, 40, and 47 bases, respectively, considering the hybridization parts, one repeating unit of H-H2-S in EDNS is around 24.9 nm; therefore, 184 numbers of repeating units H-H2-S were estimated in EDNS.

The VEGF amplifier contained an initiator strand IS-Apt$_{VEGF}$ and a cyclic reaction among H1, IS, and DNA nanostrings. IS-Apt$_{VEGF}$ recognized VEGF and released IS that is composed of the segments ab. IS was then hybridized with the hairpin-structured DNA strand H1 (a*b*cb) to form the IS-H1 duplex with unpaired segments cb (Figure 1D, step 1). The IS-H1 duplex was then reacted with EDNS via the toehold b*-mediated strand displacement reaction, which converted EDNS to a contracted configuration (CDNS), produced the H1−H2 duplex, and regenerated IS to complete the cyclic reaction process (Figure 1D, step 2, Scheme 1B). Therefore, IS was continuously produced to induce DNA nanostring configuration change, which amplified its response to VEGF. The length of 27 bp for the hairpin segments (a*b*c) in H provided sufficient length difference between the extended configuration and the contracted configuration of the DNA nanostring. To verify the proceeding of the cyclic reaction, H1 and IS were mixed with EDNS, which showed the disappearance of the H1 band and the appearance of the H1−H2 duplex band in PAGE analysis (Figure 1B, lane 7). The cyclic reaction could not proceed without the participation of IS (Figure 1B, lane 5) or H1 (Figure 1B, lane 6), and neither of them showed the appearance of the H1−H2 duplex band in PAGE analysis.

Since EDNS and CDNS demonstrated similar mobility in PAGE, DNA strand S that was labeled with TAMRA at the 3′ terminus and its corresponding quencher BHQ2 at the 5′ terminus (TAMRA-S-BHQ2) was used to synthesize the DNA nanostring for distinguishing EDNS and CDNS. The as-obtained EDNS$_{T/B}$ showed obvious TAMRA fluorescence, while CDNS$_{T/B}$ barely showed fluorescence due to the proximity of TAMRA and BHQ2 with the corresponding TAMRA fluorescence quenching (Figure 1E, EDNS$_{T/B}$, CDNS$_{T/B}$). The configuration change of the DNA nanostring was verified via monitoring the TAMRA fluorescence. Upon mixing EDNS$_{T/B}$ with IS and H1, a 6-fold TAMRA fluorescence intensity decrease was observed, indicating the conversion of EDNS$_{T/B}$ to CDNS$_{T/B}$ (Figure 1E, Figure S1A, IS, H1(+)). Only mixing EDNS$_{T/B}$ with H1 or IS did not decrease the TAMRA fluorescence intensity (Figure 1E, Figure S1A, H1 (+); IS (+)). AFM was also used to verify the CDNS structure, and the DNA nanostring demonstrated an obvious contracted structure in the presence of IS and H1, indicating efficient configuration change (Figure S2A). Height profiles of the contracted structure also showed successive peak patterns (Figure S2B), further indicating the formation of hairpins.[19]

The degree of DNA nanostring contraction was proportional to the VEGF concentration, which demonstrated a gradual decrease of the TAMRA fluorescence for VEGF in the range of 13−650 pM (Figure 1F, Amplifier (+), Figure S1C). To

https://doi.org/10.1021/jacs.2c10428
J. Am. Chem. Soc. 2023, 145, 5041−5052

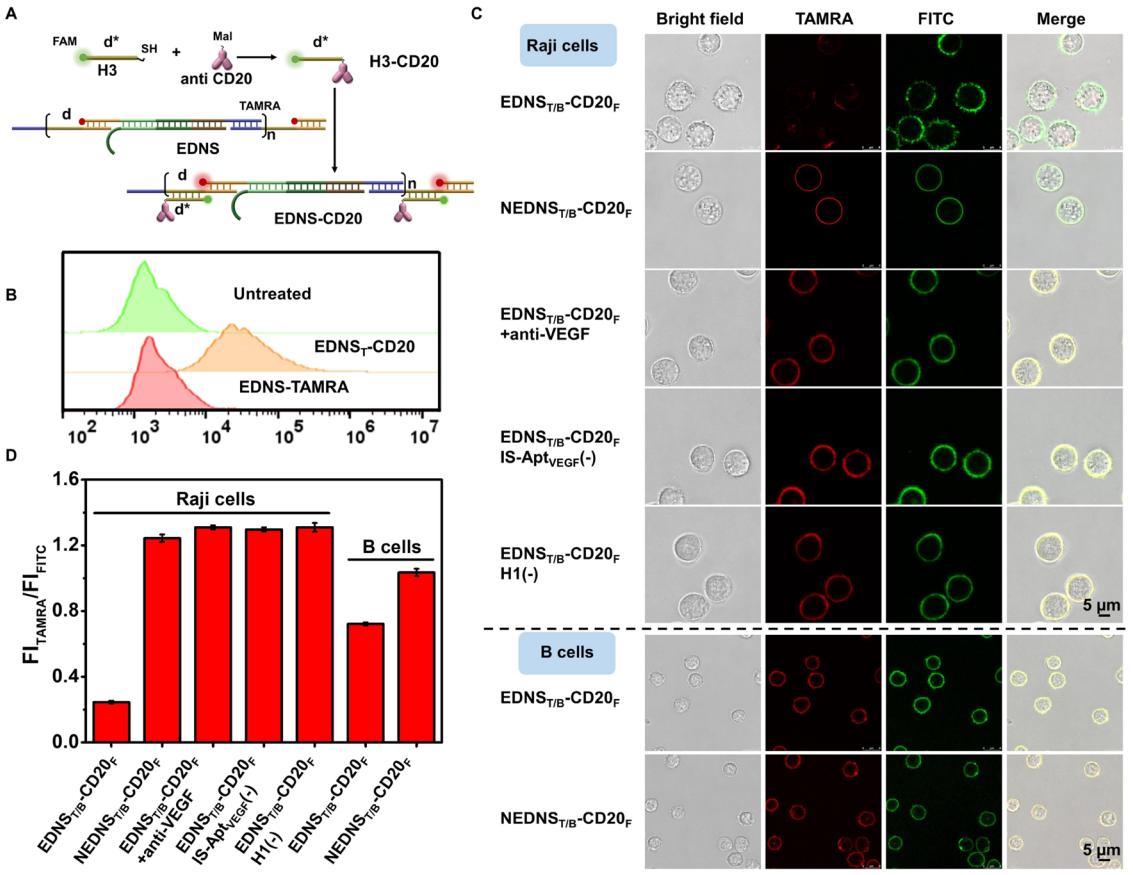

Figure 2. EDNS-CD20 synthesis and its VEGF-responsive contraction. (A) Schematic illustration of H3-CD20 synthesis and its conjugation to EDNS to obtain EDNS-CD20. (B) Flow cytometry analysis of Raji cells (Untreated) and Raji cells incubated with EDNS$_T$-CD20 (EDNS$_T$-CD20) and EDNS-TAMRA (EDNS-TAMRA) separately. (C) Confocal laser scanning microscopy (CLSM) images and (D) corresponding TAMRA/FITC fluorescence intensity ratios for Raji cells incubated with EDNS$_{T/B}$-CD20$_F$ or NEDNS$_{T/B}$-CD20$_F$, anti-VEGF pretreated Raji cells incubated with EDNS$_{T/B}$-CD20$_F$ (EDNS$_{T/B}$-CD20$_F$ + anti-VEGF), and Raji cells incubated with EDNS$_{T/B}$-CD20$_F$ and H1 (EDNS$_{T/B}$-CD20$_F$ IS-Apt$_{VEGF}$(−)) or IS-Apt$_{VEGF}$ (EDNS$_{T/B}$-CD20$_F$ H1(−)), B cells incubated with EDNS$_{T/B}$-CD20$_F$ or NEDNS$_{T/B}$-CD20$_F$. All of the above cells were co-incubated with IS-Apt$_{VEGF}$/H1 except for EDNS$_{T/B}$-CD20$_F$ IS-Apt$_{VEGF}$ (−) and EDNS$_{T/B}$-CD20$_F$ H1(−) groups.

demonstrate the contribution of the VEGF amplifier for propelling DNA nanostring configuration conversion, a control experiment was performed with IS′-Apt$_{VEGF}$, which reacted with VEGF and subsequently hybridized with H1′ to generate IS′-H1′ (Figure S1B, step 1). IS′-H1′ could also convert EDNS$_{T/B}$ to CDNS$_{T/B}$ by pulling H2 from EDNS. However, instead of regenerating to propel the cyclic reaction as IS, IS′ stayed in the IS′-H1′-H2 complex and thus could not initiate the cyclic reaction to amplify the VEGF response (Figure S1B, step 2). Therefore, the control experiment using IS′-Apt$_{VEGF}$ and H1′ demonstrated much less TAMRA signal decrease in response to the same concentration range of VEGF (Figure 1F, Amplifier (−), Figure S1D), indicating the insufficient conversion of EDNS to CDNS in the absence of the VEGF amplifier.

The above-synthesized EDNS were purified by a columnar DNA gel extraction kit to remove the low-molecular-weight products, and the as-obtained high-molecular-weight EDNS was functionalized with the CD20 antibody (anti CD20) for Raji cell anchoring. The sulfhydryl-modified DNA strand H3 (H3-SH) that has a complementary sequence (d*) to one segment (d) of the DNA strand S was conjugated with maleimide-modified anti CD20 (anti CD20-Mal), and the as-obtained H3-CD20 was then hybridized with EDNS to obtain EDNS-CD20 (Figure 2A). The successful synthesis of H3-CD20 was characterized by 10% denaturing sodium dodecyl sulfate (SDS)-PAGE gel, which demonstrated an obvious lower mobility for H3-CD20 compared with anti CD20 due to the increase of steric hindrance (Figure S3A). To further confirm the conjugation of anti CD20 to H3, FAM-labeled H3-SH (SH-H3-FAM) was used for the conjugation reaction with anti CD20-Mal. Ultrafiltration was performed after the reaction, and only weak FAM fluorescence was observed from the filtrate since the product H3-CD20-FAM was retained in the concentrate (Figure S3B, SH-H3-FAM). On the contrary, the reaction mixture of H3-FAM with anti CD20-Mal showed strong FAM fluorescence from the filtrate after ultrafiltration since H3-FAM without SH functionalization could not be conjugated to anti CD20-Mal (Figure S3B, H3-FAM).

To verify the conjugation of H3-CD20 to EDNS, the above-obtained H3-CD20-FAM was hybridized with TAMRA-labeled EDNS (EDNS-TAMRA), while FAM and TAMRA were designed with proximity location to achieve an efficient fluorescence resonance energy transfer (FRET) process in as-obtained EDNS$_T$-CD20$_F$ (Figure 2A). H3-CD20-FAM only showed FAM fluorescence (Figure S3C, H3-CD20-FAM), while EDNS$_T$-CD20$_F$ demonstrated an obvious decrease of FAM fluorescence with the appearance of TAMRA fluorescence (Figure S3C, EDNS$_T$-CD20$_F$). The successful FRET

https://doi.org/10.1021/jacs.2c10428
J. Am. Chem. Soc. 2023, 145, 5041−5052

process between FAM and TAMRA confirmed the synthesis of EDNS-CD20. Considering the molar ratio of H/H3-CD20 of 5:1 in the synthesis process, the theoretical distances between every two CD20 antibodies in EDNS and CDNS were estimated as 124.5 nm (5 × 24.9 nm) and 84 nm (5 × 16.8 nm), respectively. AFM demonstrated interval distances between CD20 antibodies of ∼130 nm for EDNS-CD20 (Figure S3D) and ∼70 nm for CDNS-CD20 (Figure S3E), which matched with the theoretical calculation results, directly confirming the contraction of the DNA nanostring.

TAMRA-labeled EDNS-CD20 ($EDNS_T$-CD20) was incubated with Raji cells and clearly showed TAMRA fluorescence around the cell membrane, which indicated the specific and efficient anchoring of $EDNS_T$-CD20 on the cell membrane (Figure 2B $EDNS_T$-CD20; Figure S4A, Raji cells, $EDNS_T$-CD20). In comparison, TAMRA fluorescence was barely observed from EDNS-TAMRA-incubated Raji cells (Figure 2B EDNS-TAMRA; Figure S4A, Raji cells, EDNS-TAMRA) or $EDNS_T$-CD20-incubated Jurkat cells that do not express CD20 on the cell membrane (Figure S4A, Jurkat cells, $EDNS_T$-CD20). As verified by western blot analysis, Raji cells and B cells have similar expression levels of CD20, while Jurkat cells have little CD20 expression (Figure S5A). Similar TAMRA fluorescence intensity was also observed from $EDNS_T$-CD20-incubated B cells and Raji cells (Figure S5B), while $EDNS_T$-CD20-incubated Jurkat cells barely showed TAMRA fluorescence (Figure S4B). TAMRA fluorescence for $EDNS_T$-CD20-treated Raji cells, B cells, and Jurkat cells was compared with untreated ones, and Raji cells and B cells showed about 10 times fluorescence difference compared with Jurkat cells, indicating satisfactory anchoring specificity of EDNS-CD20 to the Raji cell membrane and the B-cell membrane. $EDNS_T$-CD20-treated Raji cells and B cells also demonstrated similar intensity ratios of the TAMRA/membrane dye Dio, further confirming the similar affinities of EDNS-CD20 to Raji cells and B cells (Figure S5C,D).

To evaluate the contribution of VEGF on regulating CD20 receptor clustering at the cell membrane, we incubated Raji cells with EDNS-$CD20_F$ and IS-Apt_{VEGF}/H1. Even distribution of FITC fluorescence was observed on the cell membrane in the absence of VEGF (Figure S6A, VEGF (−)), while apparent FITC clusters were observed on the cell membrane in the presence of excess VEGF (Figure S6A, VEGF (+)), indicating efficient CD20 aggregation on the cell membrane. The CD20 receptor acts as a store-operated calcium channel, whose aggregation leads to the extracellular calcium influx[31] and generates cell apoptosis.[32] Fluo-4 AM, a single-wave calcium detection probe with emission intensity proportional to the concentration of Ca^{2+} binding, was used to detect calcium influx, which also indicates the extent of CD20 clustering. It demonstrated a much stronger intracellular Fluo-4 AM fluorescence in response to the external addition of excess VEGF (Figure S6B).

The capability of VEGF secretion for Raji cells and B cells was verified from cell culture supernatants via an enzyme-linked immunosorbent assay (ELISA), and Raji cells showed a superior capability of VEGF secretion (Figure S7), which guaranteed the selective contraction of EDNS on the Raji cell membrane. To verify DNA nanostring contraction on the cell membrane, $EDNS_{T/B}$ was hybridized with FITC-labeled anti CD20 to obtain $EDNS_{T/B}$-$CD20_F$. The as-obtained $EDNS_{T/B}$-$CD20_F$ was incubated with Raji cells in the presence of IS-Apt_{VEGF} and H1 and showed greatly reduced TAMRA fluorescence surrounding the cell membrane due to the proximity of BHQ2 to TAMRA, indicating the contraction of the DNA nanostring on the cell membrane. FITC fluorescence also demonstrated obvious aggregation at the cell membrane, indicating efficient CD20 clustering (Figure 2C, Raji cells, $EDNS_{T/B}$-$CD20_F$). A series of control experiments were also performed to verify VEGF-specific CD20 clustering at the cell membrane. The DNA nanostring that does not respond to VEGF ($NEDNS_{T/B}$-$CD20_F$) was incubated with Raji cells in the presence of IS-Apt_{VEGF} and H1; it did not show TAMRA fluorescence decrease, while FITC fluorescence was uniformly distributed on the cell membrane (Figure 2C, Raji cells, $NEDNS_{T/B}$-$CD20_F$). An additional control experiment was performed by pretreating VEGF with the VEGF antibody (anti-VEGF). Since anti-VEGF could block the binding of IS-Apt_{VEGF} to VEGF (Figure S8), excess anti-VEGF was used to passivate the secreted VEGF, which prevented the specific recognition of IS-Apt_{VEGF} and correspondingly incapacitated the VEGF amplifier. Incubating $EDNS_{T/B}$-$CD20_F$ and IS-Apt_{VEGF}/H1 with anti-VEGF pretreated Raji cells demonstrated strong TAMRA fluorescence surrounding Raji cells with smooth FITC fluorescence distribution at the cell membrane (Figure 2C, Raji cells, $EDNS_{T/B}$-$CD20_F$ + anti-VEGF). EDNS contraction could not proceed in the absence of either IS-Apt_{VEGF} or H1 (Figure 2C, Raji cells, $EDNS_{T/B}$-$CD20_F$, IS-Apt_{VEGF} (−); Raji cells, $EDNS_{T/B}$-$CD20_F$ H1(−)). Large numbers of cell population also demonstrated efficient TAMRA fluorescence quenching in the presence of IS-Apt_{VEGF}/H1 (Figure S6C), indicating the efficient formation of CDNS-CD20. Similar FITC fluorescence was observed from all of the treated Raji cells, indicating the efficient anchoring of $EDNS_{T/B}$-$CD20_F$ on the cell membrane.

Normal lymphocyte B cells, which also express CD20 on the cell membrane but secrete much less VEGF,[33] were also incubated with $EDNS_{T/B}$-$CD20_F$ and $NEDNS_{T/B}$-$CD20_F$. Both of the as-treated B cells showed obvious FITC fluorescence on the cell membrane, indicating successful anchoring of the DNA nanostring (Figure 2C, B cells, FITC channel). Similar to the situation for Raji cells, $NEDNS_{T/B}$-$CD20_F$-incubated B cells showed strong TAMRA fluorescence surrounding the cell membrane (Figure 2C, B cells, $NEDNS_{T/B}$-$CD20_F$). However, B cells that incubated with $EDNS_{T/B}$-$CD20_F$ only showed a very limited decrease of TAMRA fluorescence with little aggregation of FITC fluorescence due to the much fewer VEGF secretions (Figure 2C, B cells, $EDNS_{T/B}$-$CD20_F$). The TAMRA fluorescence intensity was collected from the cell membrane and ratioed over that of the FITC fluorescence intensity to quantitatively compare the DNA nanostring contraction corresponding to different treatments. $EDNS_{T/B}$-$CD20_F$ and IS-Apt_{VEGF}/H1 treatments showed a much significant decrease in the TAMRA/FITC ratio for Raji cells compared with B cells (Figure 2D), indicating that the DNA nanostring contraction only proceeded for Raji cells. Therefore, the SMARC strategy could provide satisfactory cancer cell selectivity via the VEGF amplifier in manipulating membrane receptor clustering with little interference to normal cells.

The aggregation of the CD20 membrane receptor changes its endocytic pathway from circulation to lysosome degradation.[34] To trace the fate of CD20 clusters, Raji cells were anchored with EDNS that conjugated with allophycocyanin (APC)-labeled anti CD20 (EDNS-$CD20_A$) and NEDNS that conjugated with APC-labeled anti CD20 (NEDNS-$CD20_A$)

https://doi.org/10.1021/jacs.2c10428
J. Am. Chem. Soc. 2023, 145, 5041−5052

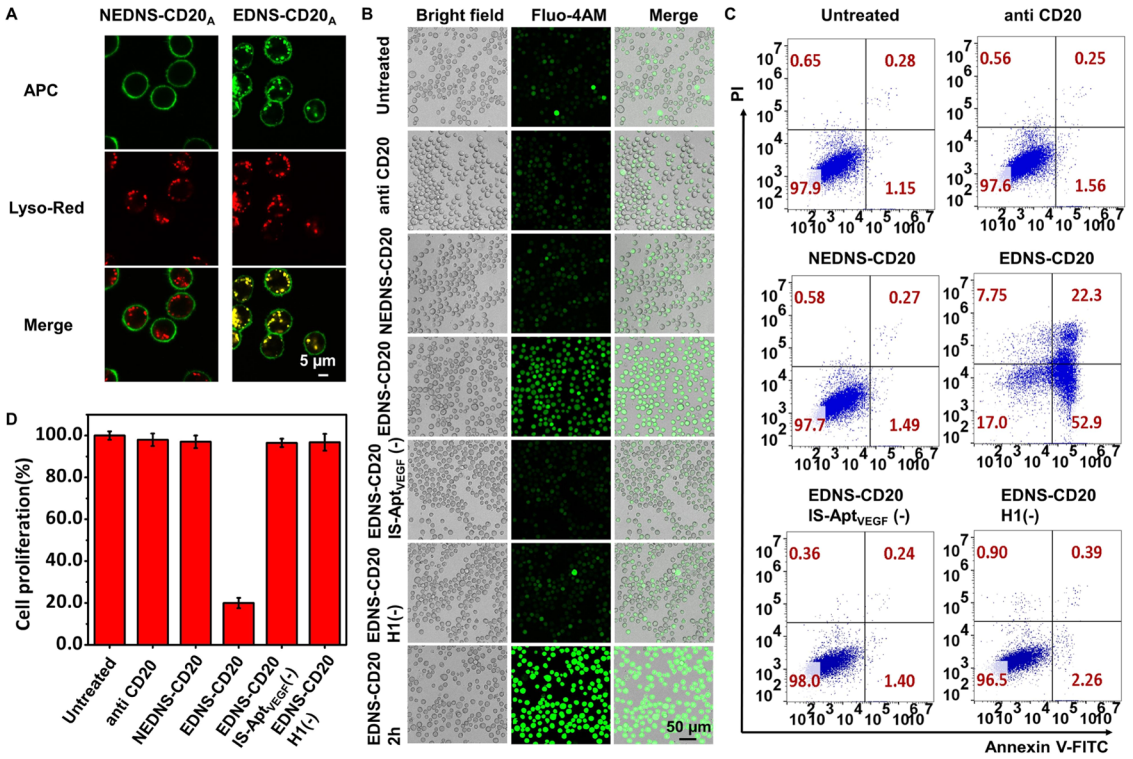

Figure 3. CD20 clustering and cell apoptosis. (A) CLSM images of Raji cells incubated with NEDNS-CD20$_A$ and EDNS-CD20$_A$ separately. The cells were co-stained with LysoTracker Red. (B) Intracellular Fluo-4 AM fluorescence, (C) flow cytometry assay, and (D) MTT assay for untreated Raji cells, Raji cells incubated with anti CD20, NEDNS-CD20, and EDNS-CD20 separately and Raji cells incubated with EDNS-CD20 and H1 (EDNS-CD20 IS-Apt$_{VEGF}$(−)) or IS-Apt$_{VEGF}$ (EDNS-CD20 H1(−)). All of the cells were co-incubated with IS-Apt$_{VEGF}$/H1 except for untreated Raji cells, EDNS-CD20 IS-Apt$_{VEGF}$ (−), and EDNS-CD20 H1(−) groups. The 2h represents the detection of Raji cells treated with EDNS-CD20 and IS-Apt$_{VEGF}$/H1 for 2 h.

and stained with LysoTracker Red for colocalization experiments. Since the CD20 monomer is a non-/slowly internalized membrane receptor, NEDNS-CD20$_A$-treated Raji cells showed complete separation of APC fluorescence and LysoTracker Red fluorescence. The APC fluorescence was evenly distributed at the cell membrane, indicating there was no aggregation or endocytosis of CD20 (Figure 3A, NEDNS-CD20$_A$). On the contrary, EDNS-CD20$_A$-treated Raji cells showed a large overlap of APC fluorescence and LysoTracker Red fluorescence intracellularly, as well as a substantial decrease of APC fluorescence at the cell membrane (Figure 3A, EDNS-CD20$_A$). This efficient lysosome accumulation confirmed the aggregation of CD20 receptors.

Intracellular Fluo-4 AM fluorescence corresponding to calcium influx was also used to evaluate CD20 clustering. Compared with untreated Raji cells (Figure 3B, Untreated), Raji cells that were incubated with anti CD20 barely showed intracellular Fluo-4 AM fluorescence (Figure 3B, anti CD20), and only very low Fluo-4 AM fluorescence was observed from NEDNS-CD20- and IS-Apt$_{VEGF}$/H1-incubated Raji cells (Figure 3B, NEDNS-CD20). Strong intracellular Fluo-4 AM fluorescence was only observed from EDNS-CD20- and IS-Apt$_{VEGF}$/H1-incubated Raji cells (Figure 3B, EDNS-CD20), with an approximately 4-fold increase in the Fluo-4 AM fluorescence compared to untreated Raji cells (as measured by ImageJ), indicating the successful initiation of calcium influx with the SMARC strategy. Calcium influx could not be activated in the absence of IS-Apt$_{VEGF}$ (Figure 3B, EDNS-CD20, IS-Apt$_{VEGF}$ (−)) or H1 (Figure 3B, EDNS-CD20, H1(−)). Flow cytometry analysis further confirmed the efficient and specific triggering of calcium influx via CD20 clustering, while NEDNS-CD20 or anti CD20-incubated Raji cells or EDNS-CD20-treated Raji cells in the absence of IS-Apt$_{VEGF}$ or H1 barely showed fluorescence change compared with untreated Raji cells (Figure S9A). Calcium influx at the early stages of CD20 receptor aggregation was also evaluated by flow cytometry (Figure S9B, 2h) and confocal microscopy imaging (Figure 3B, EDNS-CD20, 2h), both of which showed much higher intracellular Fluo-4 AM fluorescence intensities at 2 h post EDNS-CD20 and IS-Apt$_{VEGF}$/H1 treatment. In addition, the mitochondrial membrane potential was evaluated by measuring the depolarization degree of mitochondria via flow cytometry and confocal imaging. It demonstrated the largest mitochondria depolarization degree for EDNS-CD20-treated Raji cells with the highest proportion of the JC-1 monomer (green) over JC-1 aggregate (red) fluorescence (Figure S10), which indicated serious mitochondrial damage due to calcium influx.[35]

The cell apoptosis for CD20 clustering via the SMARC strategy was monitored via flow cytometry. EDNS-CD20- and IS-Apt$_{VEGF}$/H1-treated Raji cells showed 75.2% cell apoptosis (Figure 3C, EDNS-CD20), while NEDNS-CD20 or anti CD20 incubation or EDNS-CD20 incubation in the absence of IS-Apt$_{VEGF}$ or H1 barely affected cell viability (Figure 3C, NEDNS-CD20, anti CD20, Untreated, EDNS-CD20 IS-Apt$_{VEGF}$ (−), EDNS-CD20 H1(−)). In addition, the MTT assay further confirmed the above results, which demonstrated the lowest cell viability of ∼20% for EDNS-CD20- and IS-Apt$_{VEGF}$/H1-treated Raji cells (Figure 3D, EDNS-CD20), indicating VEGF-induced SMARC was promising for cancer

https://doi.org/10.1021/jacs.2c10428
J. Am. Chem. Soc. 2023, 145, 5041−5052

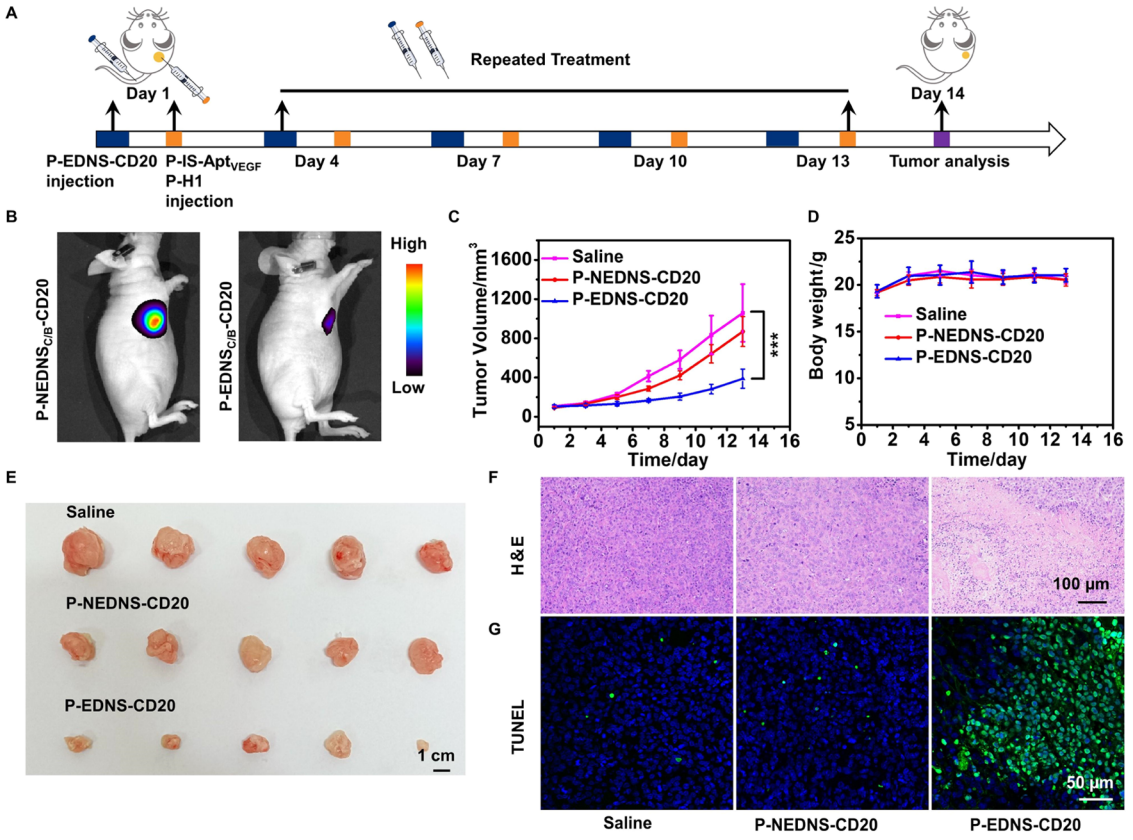

Figure 4. *In vivo* antitumor effects of the SMARC strategy. (A) Schematic illustration of treatment for subcutaneous Raji tumor mice models with five repeated injections on days 1, 4, 7, 10, and 13. (B) *In vivo* fluorescence imaging of Raji-bearing BALB/C mice injected with P-NEDNS$_{C/B}$-CD20 and P-EDNS$_{C/B}$-CD20. (C) Tumor volume change curves, (D) mice body weight, (E) photographs of dissected Raji mice tumors, (F) HE staining, and (G) TUNEL staining of Raji tumors after being treated with saline, P-NEDNS-CD20, and P-EDNS-CD20, respectively. $n = 5$ for each group. ***$P < 0.01$ for (B). Each group was also co-injected with IS-Apt$_{VEGF}$/H1 to amplify the VEGF response.

therapy. In addition, Raji cells anchored with NEDNS-CD20 still kept 97% of the cell viability (Figure 3D, NEDNS-CD20), demonstrating good biocompatibility of the DNA nanostring. Furthermore, VEGF itself does not affect cell viability, which did not generate cell apoptosis when incubating with Raji cells or B cells (Figure S11).

The therapeutic effect of the SMARC strategy was also compared to that of Rituximab (RTX), the CD20 monoclonal antibody that is FDA-approved for non-Hodgkin's lymphoma treatment.[36,37] Although RTX effectively recruits immune cells around its binding targets, its incapability in discriminating Raji cells and B cells may bring nonspecific toxicity to normal B cells. To verify it, Raji cells and normal B cells were incubated with EDNS-CD20 and RTX, respectively, and cell apoptosis was compared via the lactate dehydrogenase (LDH) release assay. The RTX-treated group was also co-incubated with NK-92MI (CD16+) cells at a ratio of 1:1 considering that it relies on the immune system to function. Both EDNS-CD20 incubation and RTX treatment demonstrated similar Raji cell apoptosis rates of ~80%. EDNS-CD20 treatment barely affected B cell viability, while RTX treatment resulted in ~55% B cell apoptosis (Figure S12). The SMARC strategy provided superior selectivity for cancer cell apoptosis and proved less impairing to normal cells.

Besides generating IS-H1 to initiate the cyclic reaction to induce DNA nanostring contraction, the specific capture of VEGF by IS-Apt$_{VEGF}$ also prevented its binding to VEGFR located on the Raji cell membrane and the human umbilical vein endothelial cell (HUVEC) membrane at the tumor position. This also contributed to cancer therapy *in vivo* by inhibiting new blood vessel growth and starving tumors of necessary oxygen and nutrients.[27] The effect of VEGF inhibition was evaluated at the cellular level by measuring the migration capability of Raji cells and HUVEC cells.[38] A transwell experiment was performed to evaluate Raji cell migration, and treating with IS-Apt$_{VEGF}$ depleted VEGF secreted by Raji cells demonstrated a reduced number of Raji cells migrated to the lower chamber compared with untreated Raji cells (Figure S13A), indicating the capability of migration inhibition. In addition, endothelial angiogenesis experiments and wound-healing assays respectively exhibited reduced tubular morphogenesis and a lower degree of wound closure for HUVEC that co-incubated with IS-Apt$_{VEGF}$-treated Raji cells compared to HUVEC that co-incubated with untreated Raji cells (Figure S13B–D). These results indicated that VEGF blocking could effectively inhibit the cell migration capability and angiogenic activity, therefore being able to contribute to cancer therapy.

To apply the SMARC strategy for *in vivo* therapy, phosphorothioate-modified DNA strands (P-DNAs), which replace one of the nonbridging oxygens of the phosphodiester linkage with sulfur to enhance metabolic stability against nuclease-mediated degradation,[39−41] were used as synthesis components for the DNA nanostring. To evaluate the stability of the DNA nanostring synthesized by P-DNAs, P-CDNS$_{T/B}$ was synthesized with P-S$_{T/B}$ that was labeled with TAMRA and

https://doi.org/10.1021/jacs.2c10428
J. Am. Chem. Soc. 2023, 145, 5041−5052

its corresponding quencher BHQ2 at the 3′ terminus and the 5′ terminus, respectively, which would recover TAMRA fluorescence upon structure disassembly (Figure S14A). Compared with $CDNS_{T/B}$, $P\text{-}CDNS_{T/B}$ showed much less TAMRA fluorescence recovery when incubated with serum (Figure S14B) and DNA exonucleases (Figure S14C), indicating good stability for *in vivo* application. The enhanced stability of P-EDNS was confirmed by PAGE analysis, which showed a stable DNA nanostring band for 48 h of 10% fetal bovine serum (FBS) treatment (Figure S14D,E). The SMARC strategy is less likely to be affected by the immune system; therefore, Raji-bearing BABL/C nude mice were chosen as mice models to evaluate the *in vivo* therapeutic effect of the SMARC strategy. Phosphorothioate-modified DNA strands were used to synthesize $P\text{-}EDNS_{C/B}$-CD20 (FigureS15A); Cy5 and its corresponding quencher BHQ3 were labeled at the 3′ terminus and 5′ terminus of P-S strand, respectively, to characterize DNA nanostring contraction *in vivo*. $P\text{-}EDNS_{C/B}$-CD20 showed strong Cy5 fluorescence due to the extended distance between Cy5 and BHQ3 (Figure S15B, VEGF (−)) and demonstrated obvious Cy5 fluorescence quenching upon VEGF recognition (Figure S15B, VEGF (+)). Raji-bearing mice were chosen as the *in vivo* models, which demonstrated an obviously higher level of VEGF expression in the tumor position than normal tissues according to the immunostaining result (Figure S16). The large difference in VEGF expression levels guarantees the selective execution of the SMARC strategy. Raji-bearing mice were intravenously injected with $P\text{-}EDNS_{C/B}$-CD20, and time-dependent Cy5 fluorescence recovery was monitored *in vivo*, which showed rapid and substantial suppression of Cy5 fluorescence at the tumor growth position. On the contrary, $P\text{-}NEDNS_{C/B}$-CD20-injected Raji-bearing mice retained strong Cy5 fluorescence at the tumor grown position (Figures 4B and S17). The effective and specific quenching of Cy5 fluorescence at the tumor grown position confirmed efficient DNA nanostring contraction *in vivo*. To evaluate the *in vivo* stability of P-EDNS-CD20, the Cy5-labeled phosphorothioated DNA scaffold ($P\text{-}EDNS_C$-CD20) (Figure S18A) was intravenously injected into Raji-bearing mice. It demonstrated accumulations and stable stay in tumor sites with strong Cy5 fluorescence during the treatment period (Figure S18B). On the contrary, Cy5-labeled EDNS without phosphorothioation ($EDNS_C$-CD20) was fast decomposed *in vivo* with the disappearance of Cy5 fluorescence in the tumor position (Figure S18C). In addition, *ex vivo* imaging was performed for the harvested organs and tumors to show the biodistribution of the DNA nanostring. Both $P\text{-}EDNS_C$-CD20 and $P\text{-}NEDNS_C$-CD20 demonstrated good tumor-targeting efficiencies (Figure S18D). To perform the pharmacokinetic study of EDNS, plasma Cy5 fluorescence was measured for $P\text{-}EDNS_C$-CD20- and $EDNS_C$-CD20-treated mice, respectively (Figure S18E). $P\text{-}EDNS_C$-CD20 demonstrated a higher level of blood retention and longer systemic circulation times than $EDNS_C$-CD20.

To evaluate the *in vivo* therapeutic efficacy of the SMARC strategy, Raji tumor-bearing mice were injected with P-EDNS-CD20 and $P\text{-IS-Apt}_{VEGF}$/P-H1 (Figure 4A), which showed a ∼70.2 or ∼63.6% reduction in tumor volume growth compared to the mice groups injected with saline or P-NEDNS-CD20 (Figure 4C,E). The control mice groups were also injected with $P\text{-IS-Apt}_{VEGF}$/P-H1 to amplify the VEGF response. Meanwhile, both TUNEL and H&E staining images also exhibited the highest level of green fluorescence and a large number of apoptosis cells for P-EDNS-CD20-injected mice, while P-NEDNS-CD20-injected mice demonstrated dense nuclei and a uniform cytoplasm with only part of the cancer cells being killed (Figure 4F,G). This result showed satisfactory *in vivo* therapeutic efficiency and specificity for the SMARC strategy. The body weights of all mice groups did not significantly fluctuate during the therapeutic period (Figure 4D). All mice groups showed no significant pathological abnormalities in their major organs including the heart, liver, lung, spleen, and kidney (Figure S19), which confirmed the good biocompatibility of the SMARC strategy.

The administration of $P\text{-IS-Apt}_{VEGF}$ and P-H1 was also performed via tail vein injections to make the SMARC strategy more appropriate for tumor therapy. The responsive DNA nanocarrier (RDNC) was synthesized by rolling circle amplification as the delivery carrier for $P\text{-IS-Apt}_{VEGF}$ and P-H1-L. P-H1-L also contained a reactive oxygen species (ROS)-responsive linker (Figure S20A). c-Met aptamers were also contained in RDNC for cancer cell recognition and precise delivery. After successive intravenous injection, P-EDNS-CD20 and RDNC bound to Raji cells separately; the recognition of VEGF released P-IS from RDNC and the tumor microenvironment ROS cleaved P-H1-L to release P-H1. P-H1-IS was therefore generated locally (Figure S20B,C), which caused efficient DNA nanostring contraction with CD20 receptors clustering at the cell membrane. The *in vivo* therapeutic effects were determined on the 14th day, which demonstrated obvious suppression of tumor growth for the P-EDNS-CD20/RDNC intravenously injected mice group (Figure S20D,E). Mice weights remained stable for two groups during the whole therapeutic process (Figure S20F). These results indicated the feasibility of intravenously administrating P-EDNS-CD20 and $P\text{-IS-Apt}_{VEGF}$/P-H1 for the SMARC strategy.

CONCLUSIONS

In summary, here, we developed a SMARC strategy of CD20 clustering selectively for lymphoma Raji cells. A retractable DNA nanostring was anchored to the cell membrane via recognizing the membrane receptor CD20. It contracted from the extended configuration upon recognizing VEGF that was secreted from cancer cells and pulled the CD20 receptor to aggregate. A VEGF amplifier containing a VEGF recognizing aptamer and a cyclic reaction further improved the contraction level of the DNA nanostring in response to VEGF secretion. The SMARC strategy selectively induced apoptosis to lymphoma Raji cells with little side effects to normal B cells. *In vivo* experiments also showed outstanding inhibitory effects on tumor growth; therefore, it has promising application potential in precise therapy.

EXPERIMENTAL SECTION

Materials. All DNAs were synthesized and purified by Sangon Biotech Co., Ltd (Shanghai, China). The sequences for all DNA strands are listed in Table S1. The CD20 antibody (anti CD20) and the FITC-labeled CD20 antibody (anti CD20-FITC) were purchased from Thermo Fisher Scientific. Recombinant human vascular endothelial growth factor 165 (VEGF) and 10× tris-borate-EDTA (TBE) buffer were purchased from Sangon Biotech Co., Ltd (Shanghai, China). NHS-PEG_2-MAL was purchased from ToYong Biotech (Shanghai, China). The annexin V-fluorescein isothiocyanate (FITC)/propidium iodide (PI) apoptosis detection kit, the JC-1 apoptosis detection kit, and Dulbecco phosphate-buffered saline (DPBS) were purchased from Keygen Biotech (Nanjing, China). Raji cell lines were obtained from Keygen Biotech (Nanjing, China).

https://doi.org/10.1021/jacs.2c10428
J. Am. Chem. Soc. 2023, 145, 5041−5052

Normal B cells were obtained from IASO Bio Therapeutics and directly used after being received.

Apparatus. The concentrations of nucleic acids were measured by a NanoDrop 2000 UV−vis spectrophotometer. AFM imaging was performed under ambient conditions using the tapping mode with a Bruker Dimension Icon atomic force microscope. The fluorescence spectra were obtained on a FluoroMax-4 fluorescence spectrophotometer (HITACHI, Japan). Cell images were obtained on a Leica SP8 STED 3× confocal microscope (Germany). Flow cytometric analysis was performed on the CytoFlex S flow cytometer (Beckman-Coulter). *In vivo* mice imaging was performed on the IVIS Lumina XR III *in vivo* imaging system (PerkinElmer).

Preparation of Anti CD20-oligonucleotide Conjugates (H3-CD20). Anti CD20 (13 μg) was incubated with NHS-PEG2-Mal (500 μg) in dimethyl sulfoxide (DMSO) at room temperature for 2 h, subsequently ultrafiltrated (MWCO of 3 kDa) to remove unreacted NHS-PEG_2-Mal, and washed with water three times to obtain maleimide-modified anti CD20 (anti CD20-Mal). The sulfhydryl-modified DNA strand H3 (H3-SH, 10 μM) was reduced using 30 mM TCEP in HEPES (pH 6.5) at room temperature for 2 h and purified via ultrafiltration (MWCO of 3 kDa). The as-treated H3-SH was then incubated with the above-obtained anti CD20-Mal at 37 °C overnight. The as-obtained H3-CD20 was ultrafiltrated (MWCO of 10 kDa) and verified with SDS-PAGE.

Synthesis of Extended DNA Nanostring-Anti CD20 (EDNS-CD20). Straight DNA strand S, straight DNA strand H2, and hairpin-structured DNA strand H were self-assembled via a hybridization reaction to synthesize the extended DNA nanostring (EDNS). 5 μL of each DNA strand (10 μM) was mixed and incubated in PBS at 95 °C for 4 min and then naturally cooled to room temperature to form EDNS. To monitor the structure change of EDNS, $EDNS_{T/B}$ was synthesized using TAMRA and its corresponding quencher BHQ2 modified DNA strand S (TAMRA-S-BHQ2) instead of S.

To synthesize the extended DNA nanostring-anti CD20 (EDNS-CD20), the above-prepared EDNS were purified by a column DNA gel extraction kit, mixed with H3-CD20 with a 5:1 molar ratio, and reacted in DPBS for 2 h at 37 °C. The as-obtained EDNS-CD20 was stored at 4 °C for future use.

***In Vitro* Verification of EDNS Response to VEGF.** Various concentrations of the recombinant VEGF (13−650 pM) were mixed with 40 μL of IS-Apt_{VEGF} (1 μM), 40 μL of H1 (1 μM), and 40 μL of $EDNS_{T/B}$ (1 μM) in 10 mM HEPES buffer (pH = 7.4, 5 mM $MgCl_2$) and incubated at 37 °C for 2 h. The corresponding decrease of the TAMRA fluorescence intensity at 580 nm was measured. To verify the contribution of the VEGF amplifier to EDNS response, a control experiment was performed using IS′-Apt_{VEGF} and H1′ that have less numbers of complementary base pairs instead of IS-Apt_{VEGF} and H1.

Gel Electrophoresis Analysis. Polyacrylamide gel electrophoresis was used to verify the reaction specificity of EDNS. An 8% native polyacrylamide gel was prepared using a 1× TBE buffer. The samples were prepared by mixing 5 μL of analyzed DNA strands with 1 μL of 6× loading buffer. Polyacrylamide gel electrophoresis was run at 120 V for 50 min in 1× TBE buffer. The gels were stained with the SYBR Gold nucleic acid gel stain (Thermo Fisher Scientific) and scanned with a molecular imager Gel Doc XR.

AFM Imaging. A total of 10 μL of analyzed DNA strands was adsorbed onto a freshly cleaved mica surface for 5 min, rinsed with deionized water 10 times, and dried with a nitrogen flow. The samples were imaged with AFM in the tapping mode.

Cell Culture. Raji and Jurkat cells were cultured in an RPMI-1640 medium complemented with 10% FBS, streptomycin (100 mg/mL), and penicillin (100 mg/mL) at 37 °C in a humidified atmosphere containing 5% CO_2. HUVEC cells were cultured in the same conditions except that Dulbecco's modified Eagle's medium (DMEM) was used as a cell culture medium instead of RPMI-1640 medium. Cell numbers were counted by a Countess II FL Automated Cell Counter (Thermo Fisher Scientific).

EDNS Response to VEGF at the Cellular Level. To monitor the VEGF-responsive structure change of EDNS on the cell membrane, 2 × 10^5 Raji cells were pretreated with 100 ng/mL LPS for 16 h to overexpress VEGF, and the supernatant of the cell culture medium was collected. Raji cells were then incubated with 1 μM $EDNS_{T/B}$-$CD20_F$ for 1 h at 37 °C (anti CD20 was labeled with FITC for colocalization experiments). Subsequently, the Raji cell culture medium was replaced with the above-collected supernatant containing cell-secreted VEGF and further incubated with IS-Apt_{VEGF} and H1 (1 μM) for 1 h at 37 °C, washed with DPBS three times, and resuspended in 200 μL of DPBS in 4-well dishes to take the CLSM fluorescence images. FITC was excited at 488 nm, and the emissions were collected from 500 to 540 nm. The fluorescence of TAMRA was observed from 565 to 620 nm under 550 nm excitation. Control experiments were performed by (1) incubating Raji cells with nonspecific EDNS that does not respond to VEGF ($NEDNS_{T/B}$-$CD20_F$), IS-Apt_{VEGF}, and H1; and (2) incubating $EDNS_T$-CD20, IS-Apt_{VEGF}, and H1 with Jurkat cells that do not express CD20 at the cell membrane. To verify the response specificity of EDNS to VEGF, Raji cells were incubated with the VEGF inhibitor (anti-VEGF) to inhibit VEGF binding to IS-Apt_{VEGF}. The as-treated Raji cells were then incubated with $EDNS_{T/B}$-$CD20_F$, IS-Apt_{VEGF}, and H1 (1 μM) for 1 h at 37 °C, washed with DPBS three times, and resuspended in 200 μL of DPBS in a single-well confocal dish before confocal visualization. In addition, 2 × 10^5 normal B cells, which only secrete a small amount of VEGF, were incubated with $EDNS_{T/B}$-$CD20_F$ (1 μM) for 1 h at 37 °C. After removing the EDNS incubation solution, the as-treated B cells were further incubated with IS-Apt_{VEGF} and H1 (1 μM) for 1 h at 37 °C, washed with DPBS three times, and resuspended in 200 μL of DPBS in 4-well dishes to take the CLSM fluorescence images. The control group for normal B cells was set by incubating with $NEDNS_{T/B}$-$CD20_F$, IS-Apt_{VEGF}, and H1.

Apoptosis Experiment. Raji cells in FBS-free 1640 medium were seeded in 1.5 mL sterile Eppendorf tubes with a volume of 200 μL per tube. The cell density was fixed at 1 × 10^6/mL, and cells were pretreated with 100 ng/mL LPS for 16 h to overexpress VEGF. EDNS-CD20 was then added into the tube to a final concentration of 1 μM. After co-incubating at 37 °C for 1 h, the cells were continuously treated with IS-Apt_{VEGF} and H1 (1 μM) for 24 h and stained with an Annexin V-FITC/PI detection kit for FACS analysis. Control experiments were performed by incubating Raji cells with (1) NEDNS-CD20 and IS-Apt_{VEGF}/H1; and (2) anti CD20 and IS-Apt_{VEGF}/H1; and untreated Raji cells were set as controls. All experiments were carried out in triplicate.

Calcium Influx Investigation. Raji cells were sequentially incubated with EDNS-CD20 for 1 h and IS-Apt_{VEGF}/H1 for 24 h. A total of 2 × 10^5 cells were loaded with the intracellular calcium indicator Fluo-4 AM (4 μM) in 200 μL of DPBS (containing 0.9 mM Ca^{2+}) for 30 min at 37 °C. Flow cytometry and confocal microscopy were applied to measure the fluorescence intensity of intracellular calcium with 488 nm excitation and 530 nm emission.

Mitochondrial Membrane Potential Measurements. Raji cells were sequentially incubated with EDNS-CD20 and IS-Apt_{VEGF}/H1 and washed twice with PBS. The above-treated cells were then uniformly suspended in a 500 μL JC-1 working solution and incubated at 37 °C with 5% CO_2 for 15 min. After incubation, the cells were collected by centrifugation at room temperature, washed twice with a 1× incubation buffer, and finally resuspended in a 500 μL 1× incubation buffer for flow analysis or confocal imaging.

Lysosome Localization Investigation. Raji cells were sequentially treated with $EDNS\text{-}CD20_A$ (1 μM) for 1 h and IS-Apt_{VEGF}/H1 (1 μM) for 6 h. Cell lysosomes were stained with LysoTracker Red (Beyotime) for 20 min at 37 °C. The cells were then washed three times with DPBS and resuspended in DPBS in a single-well dish for confocal observation. The control group was set using $NEDNS\text{-}CD20_A$ (1 μM) instead of $EDNS\text{-}CD20_F$. All experiments were carried out in triplicate.

Cell Migration assay. HUVEC cells were seeded in 6-well plates and then starved for 24 h in an FBS-free DMEM medium. The cell monolayers were scratched uniformly with a sterile 200 μL pipette tip, and the cell-seeded well plate was washed twice with medium to remove the detached cells. The width of the wound was recorded at t = 0 h. Untreated Raji cells and IS-Apt_{VEGF} treated Raji cells were

https://doi.org/10.1021/jacs.2c10428
J. Am. Chem. Soc. 2023, 145, 5041−5052

added into the HUVEC cell-seeded well plate respectively and continued incubated for 24 h. The width of the wound was recorded at t = 24 h by an inverted microscope to calculate cell migration.

Angiogenesis Assay. A total of 100 μL of Matrigel was added to each well of a 24-well plate and allowed to polymerize at 37 °C for 30 min. HUVEC cells were centrifuged to remove the supernatant DMEM media and resuspended with untreated Raji cells and IS-Apt_{VEGF}-treated Raji cells separately. A total of 9×10^4 HUVEC cells were seeded into each well. The cells were incubated at 37 °C for 4 h and observed with an inverted microscope at 40× magnification.

Transwell Migration Assay. Raji cells were seeded into the upper chamber with an 8 μm pore membrane (Costar, Corning Incorporated), and the lower chamber was filled with a growth medium supplemented with 10% FBS. Raji cells were first starved in the FBS-free 1640 medium for 24 h, treated with IS-Apt_{VEGF}, seeded in the upper chamber, and continuously cultured for 12 h. Cells that migrated through the membrane to the lower chamber were counted by cell counting plates. Untreated Raji cells were set as control and treated using the same procedure.

Lactate Dehydrogenase (LDH) Assay. B cells were cultured with NK-92MI (CD16+) cells at a ratio of 1:1 in the presence of RTX for 24 h. Raji cells were sequentially incubated with EDNS-CD20 and IS-Apt_{VEGF}/H1 for 24 h. LDH levels in the supernatant were evaluated by measuring the absorbance at 490 nm using the LDH cytotoxicity assay kit.

Synthesis of P-EDNS and Stability Verification. To adapt the DNA nanostring to *in vivo* applications, phosphorothioate-modified DNA strands S (P-S), H2 (P-H2), and H (P-H) were used to synthesize phosphorothioate-modified EDNS (P-EDNS). To verify the serum stability of the phosphorothioate-modified DNA nanostring, the fluorescent dye TAMRA and its corresponding quencher BHQ2 were modified on P-S and hybridized with P-H to make the self-quenched DNA nanostring with a contracted configuration (P-$CDNS_{T/B}$). A total of 50 μL of the as-obtained P-$CDNS_{T/B}$ or $CDNS_{T/B}$ were dispersed in 200 μL of PBS containing 10% FBS or 2 U/L DNase I, respectively, and incubated at 37 °C for 48 h. Tris-HCl containing 2 U/L DNase I was obtained by adding 0.8 μL of 2500 U/mL DNAase I (Thermo Fisher Scientific) to 1 mL of 10 mM Tris-HCl (10 mM $CaCl_2$, 10 mM $MgCl_2$, pH 7.5). The fluorescence recoveries of TAMRA were measured at 580 nm at different time points with 550 nm excitation.

Plasma Pharmacokinetics. BABL/C mice were used to examine the pharmacokinetics of P-EDNS-CD20 and EDNS-CD20. Mice were randomly divided into two groups (n = 5 per group). P-$EDNS_C$-CD20 or $EDNS_C$-CD20 was i.v.-administrated at an equal dosage. Blood samples (50 μL) were collected at varying time points (30 min, 2, 4, 12, 24, 48, and 72 h) in a container pretreated with heparin. Heparinized plasma was obtained by centrifugation at 3000 rpm in 4 °C for 15 min with subsequent Cy5 fluorescence intensity measurement. Injected amounts of P-$EDNS_C$-CD20 and $EDNS_C$-CD20 were, respectively, spiked in and incubated with freshly collected plasma for 1 h at room temperature, followed by Cy5 fluorescence intensity measurements, the values of which were used as normalization standards.

***In Vivo* Fluorescence Imaging of P-EDNS-CD20.** Raji-bearing BABL/C nude mice were used for the *in vivo* study. The mice were purchased from Pusheng Biomedical Biotech. Co., Ltd. (Nanjing, China). All *in vivo* procedures were performed in accordance with the NIH guidelines for the care and use of laboratory animals (NIH Publication no. 85-23 Rev. 1985) and approved by the Jiangsu Administration of Experimental Animals with the approval number IACUC-2205010.

To study P-EDNS-CD20 contraction *in vivo*, the fluorescent dye Cy5 and its corresponding quencher BHQ3 were modified on P-S and hybridized with P-H, P-H2, and P-H3-anti CD20 to obtain the self-quenched P-$EDNS_{C/B}$-CD20. The mice were randomly divided into three groups (n = 5 per group) and intravenously injected with 100 μL of saline, P-$EDNS_{C/B}$-CD20 (1.5 nmol), and P-$NDNS_{C/B}$-CD20 (1.5 nmol) that does not respond to VEGF separately. At 2 h after the first administration, P-IS-Apt_{VEGF}/P-H1 (0.5 nmol) was intratumorally injected, and *in vivo* Cy5 fluorescence recovery was recorded at 700 nm at different times after the P-IS-Apt_{VEGF}/P-H1 injection.

***In Vivo* Therapeutic Effect Evaluation.** To study the *in vivo* antitumor capability of the SMARC strategy, Raji-bearing BABL/C nude mice were randomly divided into three groups (n = 5 per group) and intravenously injected with 100 μL of saline, P-EDNS-CD20 (1.5 nmol), and P-NDNS-CD20 (1.5 nmol) separately. At 2 h after the first administration, P-IS-Apt_{VEGF}/P-H1 (0.5 nmol) was intratumorally injected. The same treatments were repeated on days 4, 7, 10, and 13. The tumor volume and body weight of the mice were recorded every other day. All mice were euthanized on day 14, and the tumors were dissected for H&E or TUNEL staining to evaluate the cell apoptosis level at the tumor site. In addition, major organs such as the heart, liver, spleen, lungs, and kidneys were dissected and collected for histopathological analysis to evaluate the therapeutic safety of the SMARC strategy. Tissue imaging was also performed for dissected tumor sites and major organs to verify the accumulation of P-$EDNS_C$-CD20.

Preparation of P-L-H1. To synthesize the ROS-responsive linker NHS-IE-NHS, 2,2′-[propane-2,2-diylbis(thio)] diacetic acid (2.5 mg), *N*-hydroxysuccinamide (NHS, 2.5 mg), and 1-ethyl-3-(3-dimethylaminopropyl)carbodiimide (EDC, 3.5 mg) were mixed in DMSO and stirred at room temperature for 6 h.

P-L-H1 was prepared with P-L-NH2, the above-obtained NHS-IE-NHS, and P-H1-NH2. A total of 50 μL of NHS-IE-NHS solution was pipetted into 100 μL of P-L-NH2 solution (50 μM) and stirred for 30 min at room temperature. The as-obtained mixture solution was subsequently ultrafiltrated (MWCO of 3 kDa) to remove unreacted NHS-IE-NHS, mixed with 100 μL of P-H1-NH2 solution (50 μM), and stirred at room temperature for another 2 h to obtain the P-L-H1.

Synthesis of the Responsive DNA Nanocarrier (RDNC). A mixture of phosphorylated DNA (4 μL, 100 μM) and ligation DNA (4 μL, 100 μM) was annealed at 95 °C for 4 min and then naturally cooled down to room temperature to synthesize a circular DNA template of the RCA scaffold. T4 DNA ligase (1 μL, 400 U/μL), 10× T4 DNA ligase buffer (2 μL), and ultrapure water (9 μL) were then added to the solution, and the mixed solution was incubated at 16 °C for 16 h, followed by incubating at 65 °C for 10 min to inactivate the enzyme. The reaction mixture was then cooled down and incubated with Phi29 DNA polymerase (0.2 U/μL) and dNTPs (0.1 mM) at 30 °C for 15 h in 150 μL of the 1× Phi29 reaction buffer. After the RCA reaction, the phi29 DNA polymerase was denatured by incubating at 65 °C for 10 min, and the RCA product was obtained with a DNA purification kit.

The RDNC was assembled by mixing the above synthetic RCA product (30 μL), P-IS (60 μL,10 μM), and the above-obtained P-L-H1 (60 μL) and incubating at 37 °C for 2 h. The synthesized RDNC was purified by ultrafiltration (MWCO of 100 kDa) three times.

■ ASSOCIATED CONTENT

Supporting Information

The Supporting Information is available free of charge at https://pubs.acs.org/doi/10.1021/jacs.2c10428.

Oligonucleotide sequences; list of abbreviations; and supplementary Figures S1−S20 (PDF)

■ AUTHOR INFORMATION

Corresponding Author

Ying Liu − *State Key Laboratory of Analytical Chemistry for Life Science, School of Chemistry and Chemical Engineering, Nanjing University, Nanjing 210023, China; Chemistry and Biomedicine Innovation Center, Nanjing University, Nanjing 210023, China;* orcid.org/0000-0001-5718-7804; Phone: +86-(0)25-89681918; Email: yingliu@nju.edu.cn

https://doi.org/10.1021/jacs.2c10428
J. Am. Chem. Soc. 2023, 145, 5041−5052

Authors

Shiyi Bi − *State Key Laboratory of Analytical Chemistry for Life Science, School of Chemistry and Chemical Engineering, Nanjing University, Nanjing 210023, China*

Wei Chen − *Department of Urology, Affiliated Drum Tower Hospital, Medical School of Nanjing University, Institute of Urology, Nanjing University, Nanjing 210008, China*

Yanyun Fang − *State Key Laboratory of Analytical Chemistry for Life Science, School of Chemistry and Chemical Engineering, Nanjing University, Nanjing 210023, China*

Yingfei Wang − *State Key Laboratory of Analytical Chemistry for Life Science, School of Chemistry and Chemical Engineering, Nanjing University, Nanjing 210023, China*

Qing Zhang − *Department of Urology, Affiliated Drum Tower Hospital, Medical School of Nanjing University, Institute of Urology, Nanjing University, Nanjing 210008, China*

Hongqian Guo − *Department of Urology, Affiliated Drum Tower Hospital, Medical School of Nanjing University, Institute of Urology, Nanjing University, Nanjing 210008, China;* orcid.org/0000-0002-3121-5157

Huangxian Ju − *State Key Laboratory of Analytical Chemistry for Life Science, School of Chemistry and Chemical Engineering, Nanjing University, Nanjing 210023, China;* orcid.org/0000-0002-6741-5302

Complete contact information is available at: https://pubs.acs.org/10.1021/jacs.2c10428

Author Contributions

The manuscript was written through contributions of all authors. All authors have given approval to the final version of the manuscript.

Notes

The authors declare no competing financial interest.

■ ACKNOWLEDGMENTS

The authors gratefully acknowledge the National Natural Science Foundation of China (22022405, 21974064), the Natural Science Foundation of Jiangsu Province for distinguished Young Scholars (BK20200010), and the State Key Laboratory of Analytical Chemistry for Life Science (5431ZZXM2204).

■ REFERENCES

(1) Bonnans, C.; Chou, J.; Werb, Z. Remodelling the Extracellular Matrix in Development and Disease. *Nat. Rev. Mol. Cell Biol.* **2014**, *15*, 786−801.

(2) Zhang, K.; Deng, R.; Sun, Y.; Zhang, L.; Li, J. Reversible Control of Cell Membrane Receptor Function Using DNA Nano-Spring Multivalent Ligands. *Chem. Sci.* **2017**, *8*, 7098−7105.

(3) Chen, S.; Xu, Z.; Yang, W.; Lin, X.; Li, J.; Li, J.; Yang, H. Logic-Gate-Actuated DNA-Controlled Receptor Assembly for the Programmable Modulation of Cellular Signal Transduction. *Angew. Chem., Int. Ed.* **2019**, *58*, 18186−18190.

(4) Gowrishankar, K.; Ghosh, S.; Saha, S.; C, R.; Mayor, S.; Rao, M. Active Remodeling of Cortical Actin Regulates Spatiotemporal Organization of Cell Surface Molecules. *Cell* **2012**, *149*, 1353−1367.

(5) Spencer, D. M.; Wandless, T. J.; Schreiber, S. L.; Crabtree, G. R. Controlling signal transduction with synthetic ligands. *Science* **1993**, *262*, 1019−1024.

(6) Kiessling, L. L.; Gestwicki, J. E.; Strong, L. E. Synthetic Multivalent Ligands as Probes of Signal Transduction. *Angew. Chem., Int. Ed.* **2006**, *45*, 2348−2368.

(7) Wang, Y.; Baars, I.; Fördös, F.; Högberg, B. Clustering of Death Receptor for Apoptosis Using Nanoscale Patterns of Peptides. *ACS Nano* **2021**, *15*, 9614−9626.

(8) Li, L.; Wang, J.; Li, Y.; Radford, D. C.; Yang, J.; Kopeček, J. Broadening and Enhancing Functions of Antibodies by Self-Assembling Multimerization at Cell Surface. *ACS Nano* **2019**, *13*, 11422−11432.

(9) Li, L.; Yang, J.; Wang, J.; Kopeček, J. Amplification of CD20 Cross-Linking in Rituximab-Resistant B-Lymphoma Cells Enhances Apoptosis Induction by Drug-Free Macromolecular Therapeutics. *ACS Nano* **2018**, *12*, 3658−3670.

(10) Liu, Z.; Liu, Y.; Chang, Y.; Seyf, H. R.; Henry, A.; Mattheyses, A. L.; Yehl, K.; Zhang, Y.; Huang, Z.; Salaita, K. Nanoscale Optomechanical Actuators for Controlling Mechanotransduction in Living Cells. *Nat. Methods* **2016**, *13*, 143−146.

(11) Qi, J.; Li, W.; Xu, X.; Jin, F.; Liu, D.; Du, Y.; Wang, J.; Ying, X.; You, J.; Du, Y.; Ji, J. Cyto-Friendly Polymerization at Cell Surfaces Modulates Cell Fate by Clustering Cell-Surface Receptors. *Chem. Sci.* **2020**, *11*, 4221−4225.

(12) Mamuti, M.; Wang, Y.; Zhao, Y.; Wang, J.; Wang, J.; Fan, Y.; Xiao, W.; Hou, D.; Yang, J.; Zheng, R.; An, H.; Wang, H. A Polyvalent Peptide CD40 Nanoagonist for Targeted Modulation of Dendritic Cells and Amplified Cancer Immunotherapy. *Adv. Mater.* **2022**, *34*, No. 2109432.

(13) Smith, A.-S.; Sengupta, K.; Goennenwein, S.; Seifert, U.; Sackmann, E. Force-Induced Growth of Adhesion Domains Is Controlled by Receptor Mobility. *Proc. Natl. Acad. Sci. U.S.A.* **2008**, *105*, 6906−6911.

(14) Zhang, K.; Gao, H.; Deng, R.; Li, J. Emerging Applications of Nanotechnology for Controlling Cell-Surface Receptor Clustering. *Angew. Chem., Int. Ed.* **2019**, *58*, 4790−4799.

(15) Li, H.; Wang, M.; Shi, T.; Yang, S.; Zhang, J.; Wang, H.-H.; Nie, Z. A DNA-Mediated Chemically Induced Dimerization (D-CID) Nanodevice for Nongenetic Receptor Engineering to Control Cell Behavior. *Angew. Chem., Int. Ed.* **2018**, *57*, 10226−10230.

(16) Wang, M.; He, F.; Li, H.; Yang, S.; Zhang, J.; Ghosh, P.; Wang, H.-H.; Nie, Z. Near-Infrared Light-Activated DNA-Agonist Nanodevice for Nongenetically and Remotely Controlled Cellular Signaling and Behaviors in Live Animals. *Nano Lett.* **2019**, *19*, 2603−2613.

(17) Wang, L.; Liang, H.; Sun, J.; Liu, Y.; Li, J.; Li, J.; Li, J.; Yang, H. Bispecific Aptamer Induced Artificial Protein-Pairing: A Strategy for Selective Inhibition of Receptor Function. *J. Am. Chem. Soc.* **2019**, *141*, 12673−12681.

(18) Ueki, R.; Atsuta, S.; Ueki, A.; Sando, S. Nongenetic Reprogramming of the Ligand Specificity of Growth Factor Receptors by Bispecific DNA Aptamers. *J. Am. Chem. Soc.* **2017**, *139*, 6554−6557.

(19) Sethi, S.; Hidaka, K.; Sugiyama, H.; Endo, M. Non-invasive Regulation of Cellular Morphology Using a Photoswitchable Mechanical DNA Polymer. *Angew. Chem., Int. Ed.* **2021**, *60*, 20342−20349.

(20) Younes, A. Beyond Chemotherapy: New Agents for Targeted Treatment of Lymphoma. *Nat. Rev. Clin. Oncol.* **2011**, *8*, 85−96.

(21) Chaudhari, K.; Rizvi, S.; Syed, B. A. Non-Hodgkin Lymphoma Therapy Landscape. *Nat. Rev. Drug Discovery* **2019**, *18*, 663−664.

(22) Tedder, T. F.; Streuli, M.; Schlossman, S. F.; Saito, H. Isolation and Structure of a CDNA Encoding the B1 (CD20) Cell-Surface Antigen of Human B Lymphocytes. *Proc. Natl. Acad. Sci. U.S.A.* **1988**, *85*, 208−212.

(23) Abdulkadir, S.; Li, C.; Jiang, W.; Zhao, X.; Sang, P.; Wei, L.; Hu, Y.; Li, Q.; Cai, J. Modulating Angiogenesis by Proteomimetics of Vascular Endothelial Growth Factor. *J. Am. Chem. Soc.* **2022**, *144*, 270−281.

(24) Li, J.; Kataoka, K. Chemo-Physical Strategies to Advance the *in Vivo* Functionality of Targeted Nanomedicine: The Next Generation. *J. Am. Chem. Soc.* **2021**, *143*, 538−559.

(25) Hutchinson, L. New VEGF Model-Based Biomarker. *Nat. Rev. Clin. Oncol.* **2013**, *10*, 366.

(26) Fredriksson, S.; Dixon, W.; Ji, H.; Koong, A. C.; Mindrinos, M.; Davis, R. W. Multiplexed Protein Detection by Proximity Ligation for Cancer Biomarker Validation. *Nat. Methods* **2007**, *4*, 327−329.
(27) Ellis, L. M.; Hicklin, D. J. VEGF-Targeted Therapy: Mechanisms of Anti-Tumour Activity. *Nat. Rev. Cancer* **2008**, *8*, 579−591.
(28) Ng, E. W. M.; Shima, D. T.; Calias, P.; Cunningham, E. T.; Guyer, D. R.; Adamis, A. P. Pegaptanib, a Targeted Anti-VEGF Aptamer for Ocular Vascular Disease. *Nat. Rev. Drug Discovery* **2006**, *5*, 123−132.
(29) Zhang, P.; Fischer, A.; Ouyang, Y.; Wang, J.; Sohn, Y. S.; Nechushtai, R.; Pikarsky, E.; Fan, C.; Willner, I. Aptamer-Modified DNA Tetrahedra-Gated Metal−Organic Framework Nanoparticle Carriers for Enhanced Chemotherapy or Photodynamic Therapy. *Chem. Sci.* **2021**, *12*, 14473−14483.
(30) Liao, W.-C.; Sohn, Y. S.; Riutin, M.; Cecconello, A.; Parak, W. J.; Nechushtai, R.; Willner, I. The Application of Stimuli-Responsive VEGF- and ATP-Aptamer-Based Microcapsules for the Controlled Release of an Anticancer Drug, and the Selective Targeted Cytotoxicity toward Cancer Cells. *Adv. Funct. Mater.* **2016**, *26*, 4262−4273.
(31) Janas, E.; Priest, R.; Wilde, J. I.; White, J. H.; Malhotra, R. Rituxan (Anti-CD20 Antibody)-Induced Translocation of CD20 into Lipid Rafts Is Crucial for Calcium Influx and Apoptosis. *Clin. Exp. Immunol.* **2005**, *139*, 439−446.
(32) Mattson, M. P.; Chan, S. L. Calcium Orchestrates Apoptosis. *Nat. Cell Biol.* **2003**, *5*, 1041−1043.
(33) Motz, G. T.; Coukos, G. The Parallel Lives of Angiogenesis and Immunosuppression: Cancer and Other Tales. *Nat. Rev. Immunol.* **2011**, *11*, 702−711.
(34) Moody, P. R.; Sayers, E. J.; Magnusson, J. P.; Alexander, C.; Borri, P.; Watson, P.; Jones, A. T. Receptor Crosslinking: A General Method to Trigger Internalization and Lysosomal Targeting of Therapeutic Receptor:Ligand Complexes. *Mol. Ther.* **2015**, *23*, 1888−1898.
(35) Jambrina, E.; Alonso, R.; Alcalde, M.; del Carmen Rodríguez, M.; Serrano, A.; Martínez-A, C.; García-Sancho, J.; Izquierdo, M. Calcium Influx through Receptor-Operated Channel Induces Mitochondria-Triggered Paraptotic Cell Death. *J. Biol. Chem.* **2003**, *278*, 14134−14145.
(36) Boye, J.; Elter, T.; Engert, A. An Overview of the Current Clinical Use of the Anti-CD20 Monoclonal Antibody Rituximab. *Ann. Oncol.* **2003**, *14*, 520−535.
(37) Voelker, R. A First in Non-Hodgkin Lymphoma Treatment. *JAMA* **2019**, *321*, 23.
(38) Oommen, S.; Gupta, S. K.; Vlahakis, N. E. Vascular Endothelial Growth Factor A (VEGF-A) Induces Endothelial and Cancer Cell Migration through Direct Binding to Integrin A9β1. *J. Biol. Chem.* **2011**, *286*, 1083−1092.
(39) Eckstein, F. Phosphorothioates, Essential Components of Therapeutic Oligonucleotides. *Nucleic Acid Ther.* **2014**, *24*, 374−387.
(40) Wan, W. B.; Seth, P. P. The Medicinal Chemistry of Therapeutic Oligonucleotides. *J. Med. Chem.* **2016**, *59*, 9645−9667.
(41) Hyjek-Składanowska, M.; Vickers, T. A.; Napiórkowska, A.; Anderson, B. A.; Tanowitz, M.; Crooke, S. T.; Liang, X.; Seth, P. P.; Nowotny, M. Origins of the Increased Affinity of Phosphorothioate-Modified Therapeutic Nucleic Acids for Proteins. *J. Am. Chem. Soc.* **2020**, *142*, 7456−7468.

https://doi.org/10.1021/jacs.2c10428
J. Am. Chem. Soc. 2023, 145, 5041−5052